Global dynamics of non-equilibrium gliding in animals

Bioinspiration & Biomimetics

Global dynamics of non-equilibrium gliding in animals

Isaac J Yeaton[1], **John J Socha**[2] **and Shane D Ross**[2]

1   Department of Mechanical Engineering Virginia Tech Blacksburg, VA United States of America
2   Department of Biomedical Engineering and Mechanics Virginia Tech Blacksburg, VA United States of America

E-mail: iyeaton@vt.edu

Abstract

Gliding flight—moving horizontally downward through the air without power—has evolved in a broad diversity of taxa and serves numerous ecologically relevant functions such as predator escape, expanding foraging locations, and finding mates, and has been suggested as an evolutionary pathway to powered flight. Historically, gliding has been conceptualized using the idealized conditions of equilibrium, in which the net aerodynamic force on the glider balances its weight. While this assumption is appealing for its simplicity, recent studies of glide trajectories have shown that equilibrium gliding is not the norm for most species. Furthermore, equilibrium theory neglects the aerodynamic differences between species, as well as how a glider can modify its glide path using control. To investigate non-equilibrium glide behavior, we developed a reduced-order model of gliding that accounts for self-similarity in the equations of motion, such that the lift and drag characteristics alone determine the glide trajectory. From analysis of velocity polar diagrams of horizontal and vertical velocity from several gliding species, we find that pitch angle, the angle between the horizontal and chord line, is a control parameter that can be exploited to modulate glide angle and glide speed. Varying pitch results in changing locations of equilibrium glide configurations in the velocity polar diagram that govern passive glide dynamics. Such analyses provide a new mechanism of interspecies comparison and tools to understand experimentally-measured kinematics data and theory. In addition, this analysis suggests that the lift and drag characteristics of aerial and aquatic autonomous gliders can be engineered to passively alter glide trajectories with minimal control effort.

1. Introduction

Animal gliders move horizontally through the air by exchanging potential energy for kinetic energy and by producing and controlling aerodynamic forces [1, 2]. To meet ecologically relevant goals, including predator escape, moving to new foraging locations, searching for mates, or avoiding the forest floor, the glider must control lift and drag forces to dynamically change the glide path and landing location. Glide dynamics have generally been studied using the limited theoretical framework of equilibrium, in which the glide path is straight and performance only depends on a constant lift-to-drag ratio. However, real glide paths are not straight, and lift-to-drag ratio can vary continuously with angle of attack. How animal gliders use their unique morphologies to achieve ecological goals cannot be answered from the equilibrium framework, as it neglects transient dynamics and angle

of attack-dependent force coefficients. Furthermore, the evolution of lift-producing wing-like structures, which has occurred over thirty times in arboreal vertebrates [2], suggests that producing and controlling aerodynamic forces is selectively advantageous. To truly understand the gliding behavior of animals, then, suggests that a non-equilibrium framework is required. Here, we conceptualize glide dynamics using lift and drag coefficients that depend on angle of attack and control, which allows the angle of attack to actively vary. These refinements to previous modeling enables a more realistic view of gliding.

The equilibrium gliding assumption states that the resultant aerodynamic force balances the gravitational force. In this condition, the velocity is constant, the glide path is straight and angled down from the horizontal at a constant glide angle, and the glide angle and the lift-to-drag ratio are related by $\cot \gamma = F_L/F_D$ [3]. This assumption has been used to compare gliders and make

predictions of performance. For example, heavier individuals with higher wing loading should glide faster than lighter individuals, but both should have the same equilibrium glide angle [3]. Equilibrium theory also predicts that glide range and energy conversion efficiency will be maximized when the lift-to-drag ratio is maximized [4]. These predictions should be valid for any glider, even though species vary greatly in their size, morphology, and diversity of aerodynamic structures. Examples of this diversity include the dorsoventrally flattened body of gliding snakes [5–9], the inter-limb patagial membrane of gliding mammals [10, 11], the rib-wings of gliding lizards [12, 13], the webbed feet of gliding frogs [14], and body/limbs in wingless hexapods [15, 16] and arachnids [17].

However, there is limited evidence of equilibrium gliding in experimental studies. In one study, 52% of *Draco* glides did not reach equilibrium [13]. In experiments with the flying snake *Chrysopelea paradisi*, only one of 14 glide trials originating from a height of 9.6 m appeared to reach equilibrium [18], and no equilibrium glides were found in eight glide trials beginning from a height of 15 m [5]. Two studies of gliders recorded in the wild found similar results. Body-mounted accelerometers attached to gliding colugos generally indicated greater vertical forces than required for equilibrium [11], and no equilibrium glides were found in long horizontal distance (18 m) glides of northern flying squirrels, *Glaucomys sabrinus*. Simulated glides of *G. sabrinus* required time-varying force coefficients to reproduce the observed trajectories in this species [10]. These studies show that non-equilibrium gliding is dominant in real trajectories.

Observations of non-equilibrium gliding are not unexpected given the coupled effects of animal behavior and aerodynamic force production on glide trajectories. All gliders must accelerate to sufficient velocities to produce appreciable aerodynamic forces, so there is always some non-equilibrium portion at the start of any glide. Similarly, slowing the glide before landing and controlling contact with the substrate requires aerodynamic and postural changes [19]. An animal can also modify force production by changing the wing itself, by varying the camber or aspect ratio with relative limb position [20, 21]. Furthermore, gliders can maneuver volitionally, or make small adjustments to the trajectory to achieve a goal such as landing on a targeted tree [22].

The other source of complexity that can affect glide dynamics is the local airflow interaction with the body. During the ballistic and shallowing phases of gliding that precede equilibrium, the relative air velocity changes continuously in magnitude and in direction. Lift and drag forces scale as the velocity squared, and their lines-of-action depend on the instantaneous flow direction. Additionally, lift and drag coefficients depend strongly on the animal's angle of attack, which changes passively as the glide angle changes, and actively if the animal changes its pitch angle using control. Understanding this coupling of animal behavior and force

production requires not only kinematics and force coefficient data, but also modeling to unify experimental observations with physical theory.

Theoretical models have been used to study the effects of force coefficients, wing loading, and initial conditions on glider performance and stability. Models from the late 1800's were developed to understand bird flight [23, 24], but more recent modeling work can be categorized as either particle models or rigid-body models. Particle models consider the glider as a point mass moving in the vertical plane under the influence of lift, drag, and gravity [4, 5, 10, 25]. These models decouple the instantaneous lift and drag coefficients from the glide dynamics, by assuming that the coefficients are either constants or arbitrary functions of time, but not functions of angle of attack. A dominant feature revealed from particle models is damped oscillations in velocity, acceleration, and glide angle time series before the glider reaches equilibrium [4, 5, 24, 25]. Rigid-body models couple both the translational and rotational pitch dynamics of the glider. Jafari *et al* [26] developed two tandem-wing rigid-body models to investigate the passive stability characteristics of flying snakes [26], finding that stable glides are possible, but depend on the initial conditions of pitch and pitch rate. Certain combinations of initial conditions lead to equilibrium glides, whereas other combinations lead to falling with a negligible horizontal velocity.

Here, we used theoretical modeling and a new analysis of the velocity polar diagram (*sensu* Tucker [27]) of horizontal versus vertical velocity to develop a non-equilibrium theoretical framework to understand the mechanics of gliding. This work was specifically motivated by the question, what is the effect of angle-of-attack-dependent lift and drag coefficients on a glider's trajectory dynamics? We developed a rigid-body model using a new rescaling to isolate the effects of the lift and drag coefficients. This rescaling enabled us to test the effect of lift and drag coefficients using simulated glides, with angle-of-attack-dependent force coefficients taken from previous studies. In particular, we used force coefficients from studies of flying squirrels [10, 20], flying snakes [8], sugar gliders [28], flying fish [29], chukar partridge [30] and dragonflies [31]. This broad sampling of animals helps to elucidate commonalities of non-equilibrium gliding, demonstrating the utility of this non-equilibrium framework across phylogenetically diverse species. As future kinematics studies reveal more detailed glide information, this framework can be used to answer questions about how gliders control the trajectory by varying body posture.

2. Methods

We formulate the equations of motion for a glider translating in the vertical *x-z* plane (figure 1(e)) under the influence of lift, drag, and gravity. We analyze the glider as a rigid body in which angle of attack changes with glide angle and a specified body pitch angle. That is,
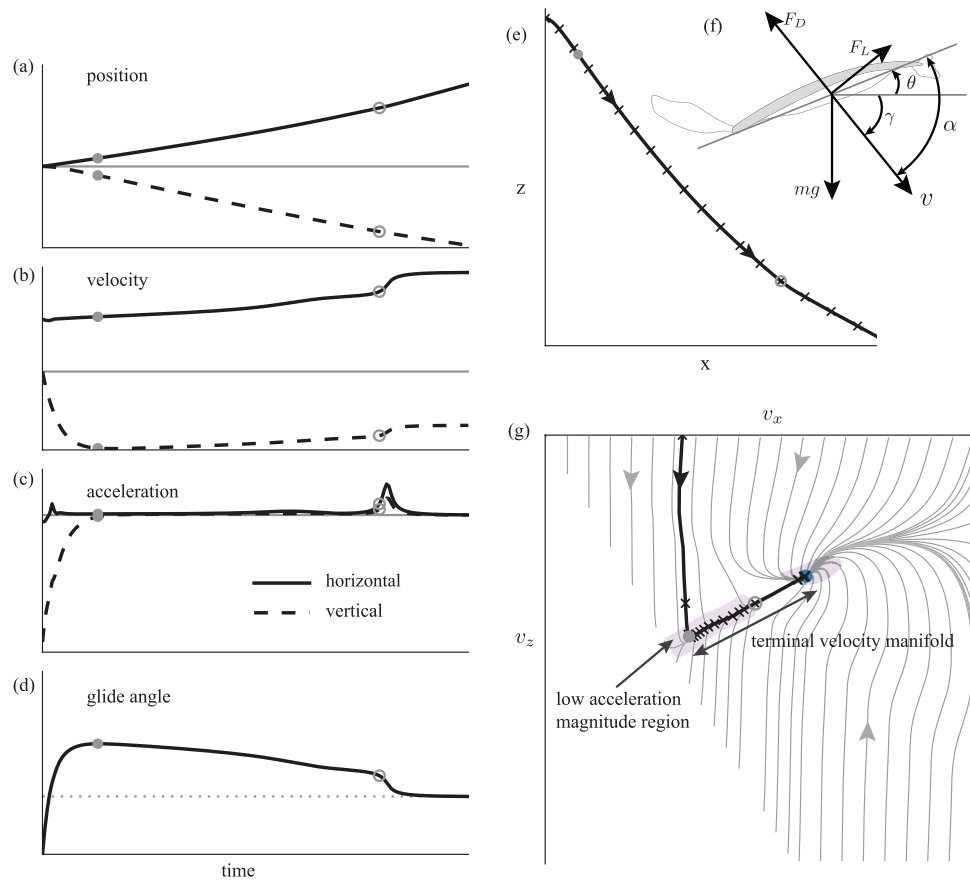
Figure 1. Construction of the velocity polar diagram. (a)–(d) Time histories of position, velocity, acceleration, and glide angle from one simulated glide. The solid circle denotes the location of maximum glide angle, marking the end of the ballistic phase. The open circle denotes an increase in acceleration near the end of the trajectory. The dashed line in (d) indicates the equilibrium glide angle, γ^*. (e) Horizontal (x) and vertical (z) glide path of the simulated glider, where equally spaced points in time are indicated by the 'x' markers, and arrows indicate the direction of forward travel. (f) Schematic of the rigid-body glider model with pitch control analyzed and simulated in this study. (g) Velocity polar diagram, with the simulated trajectory overlaid in black and motion in forward time indicated by the arrow on the trajectory. Gray lines indicate trajectories with different initial conditions of velocity. The end of the ballistic phase occurs when the velocity trajectory transitions onto the terminal velocity manifold. The terminal velocity manifold is surrounded by a low acceleration magnitude region, $\sqrt{a_x^2 + a_z^2} < 0.1\,\mathrm{g}$, indicated by the purple shading. The animal accelerates along the manifold, indicated by loss of shading and denoted with the open circle. The stable equilibrium is denoted by the blue circle; the equilibrium glide angle is the angle subtended between the horizontal axis and a line from the origin to the equilibrium point. The empty wedge-shaped area results from of the angle of attack limitations of the experimentally measured lift and drag coefficients (see supplemental information (stacks.iop.org/BB/12/026013/mmedia)).

we do not write an equation of motion for the rotational dynamics, but instead use the pitch angle to elicit different system responses. To encapsulate a glider's motion in an intuitive and informative manner, we use the velocity polar diagram (figure 1(g)) instead of time series of position, velocity, acceleration, and glide angle (figures 1(a)–(d)). The velocity, acceleration, and glide angle information is embedded in the diagram, and equilibrium gliding can be clearly identified as points where the acceleration vector goes to zero and to which velocity trajectories are attracted to or repelled from.

2.1. Rigid-body model equations of motion

Using the free-body diagram in figure 1(f) for a glider of mass m in an inertial reference frame defined by x and z, we write the equations of motion in the horizontal and vertical directions as

$$m\dot{v}_x = F_L \sin\gamma - F_D \cos\gamma$$
$$m\dot{v}_z = F_L \cos\gamma + F_D \sin\gamma - mg, \qquad (2.1)$$

where the overdot signifies the time derivative, F_L and F_D are the lift and drag forces, v_x and v_z are the velocities in the horizontal and vertical directions, and $a_x = \dot{v}_x$ and $a_z = \dot{v}_z$ are the accelerations in the horizontal and vertical directions. The instantaneous glide angle, $\gamma = -\tan^{-1} v_z/v_x$, is defined as positive for a clockwise rotation from the horizontal axis (i.e. the glide angle will be positive when the animal glides downward). By definition, the drag force acts counter to the local direction of forward travel along the glide trajectory, lift force acts normal to it, and both are written as

$$F_L = \frac{\rho v^2}{2} S C_L(\alpha), \quad F_D = \frac{\rho v^2}{2} S C_D(\alpha), \quad (2.2)$$

where ρ is air density, $v = \sqrt{v_x^2 + v_z^2}$ is airspeed, S is projected surface area of the glider, $\alpha = \gamma + \theta$ is angle of attack, and θ is pitch angle, which specifies the angle between the mean chord line and the horizontal axis (positive counter-clockwise from the horizontal).

Pitch angle is a free parameter in the model, whereas glide angle is not.

The lift and drag coefficients, $C_L(\alpha)$ and $C_D(\alpha)$, are functions of angle of attack in this model, as determined from lift and drag curves specific to each glider. In general, these curves depend on airfoil shape and Reynolds number [32], and must be determined experimentally. For this analysis, we chose characteristic lift and drag curves for a particular Reynolds number and wing shape, using angle of attack as the only free parameter that determines the instantaneous lift and drag coefficients. Although the lift and drag coefficients are velocity-independent, the lift and drag forces are not. Combining equations (2.1) and (2.2), we arrive at the following expression for the glider's accelerations,

$$\dot{v}_x = \frac{\rho v^2}{2} \frac{S}{m} \left[C_L(\alpha) \sin\gamma - C_D(\alpha)\cos\gamma \right] \quad (2.3)$$

$$\dot{v}_z = \frac{\rho v^2}{2} \frac{S}{m} \left[C_L(\alpha) \cos\gamma + C_D(\alpha)\sin\gamma \right] - g \quad (2.4)$$

2.2. Dimensional analysis

We non-dimensionalize the equations of motion using the chord length c as the characteristic length scale. For a flying snake, the chord length is nominally the flattened aerial width of the animal [5, 8], and for a gliding mammal, it is the distance between the wrist and the ankle along the stretched patagium [21, 33]. The non-dimensional time scale, $T = \sqrt{c/g}$, is found by normalizing by the gravitational acceleration g; it follows that the characteristic velocity scale is $c/T = \sqrt{cg}$. We define the non-dimensional time, velocity, and positions as

$$\bar{t} = \frac{t}{\sqrt{c/g}}, \quad \bar{v} = \frac{v}{\sqrt{cg}}, \quad \bar{p} = \frac{p}{c}.$$

where v is either v_x or v_z and p is either x or z. After substituting the non-dimensional groups into the equations of motion (2.3) and (2.4), we find

$$\frac{d\bar{v}_x}{d\bar{t}} = \epsilon \bar{v}^2 \left[C_L(\alpha) \sin\gamma - C_D(\alpha)\cos\gamma \right]$$

$$\frac{d\bar{v}_z}{d\bar{t}} = \epsilon \bar{v}^2 \left[C_L(\alpha) \cos\gamma + C_D(\alpha)\sin\gamma \right] - 1$$

where the non-dimensional parameter ϵ can be cast in terms of wing loading, $W_S = mg/S$, as

$$\epsilon = \frac{\rho c}{2} \frac{S}{m} = \frac{\rho g}{2} \frac{c}{W_S}$$

We define ϵ as the universal glide scaling parameter and discuss its significance in section 4.2.

2.3. Rescaling and final equation form

The non-dimensional equations can be further simplified by rescaling velocity and time as $\hat{v} = \sqrt{\epsilon}\,\bar{v}$ and $\hat{t} = \sqrt{\epsilon}\,\bar{t}$. Writing completely in terms of $\hat{v}_x = \hat{v}\cos\gamma$

and $\hat{v}_z = -\hat{v}\sin\gamma$, the Cartesian form of the equations of motion is

$$\hat{v}_x' = -\sqrt{\hat{v}_x^2 + \hat{v}_z^2}\, \left[C_L(\alpha)\hat{v}_z + C_D(\alpha)\hat{v}_x \right] \quad (2.5)$$

$$\hat{v}_z' = \sqrt{\hat{v}_x^2 + \hat{v}_z^2}\, \left[C_L(\alpha)\hat{v}_x - C_D(\alpha)\hat{v}_z \right] - 1 \quad (2.6)$$

where prime notation is used as a shorthand for rescaled time derivatives $\frac{d}{d\hat{t}}$. These equations are integrated to construct the velocity polar diagram trajectories. The polar form of the equations, written in terms of the airspeed $\hat{v} = \sqrt{\hat{v}_x^2 + \hat{v}_z^2}$ and glide angle $\gamma = -\tan^{-1}\hat{v}_z/\hat{v}_x$, is

$$\gamma' = -\hat{v}C_L(\alpha) + \frac{\cos\gamma}{\hat{v}} \quad (2.7)$$

$$\hat{v}' = -\hat{v}^2 C_D(\alpha) + \sin\gamma \quad (2.8)$$

Note that the rescaled equations do not depend on body size or wing loading, but only on the lift and drag coefficients. Therefore, any differences in glide performance must result from differences in the lift and drag curves.

2.4. Equilibrium gliding

Equilibrium gliding occurs when the resultant aerodynamic force balances the gravitational force on the glider, producing a constant glide angle and speed. This condition requires that the left-hand sides of expressions (2.5) to (2.8) are zero, resulting in the equilibrium states $(\hat{v}_x^*, \hat{v}_z^*)$ and $(\gamma^*, \hat{v}^*)$. Once the equilibrium glide angle γ^* is known, the equilibrium airspeed $\hat{v}^*$ is determined from equations (2.7) or (2.8), and the equilibrium horizontal and vertical velocities are found using $\hat{v}_x^* = \hat{v}^*\cos\gamma^*$ and $\hat{v}_z^* = -\hat{v}^*\sin\gamma^*$. Simple algebraic manipulation of the equilibrium equations of motion results in the well-known expression for the equilibrium glide angle

$$\frac{F_L}{F_D} = \frac{C_L(\alpha^*)}{C_D(\alpha^*)} = \frac{C_L(\gamma^* + \theta)}{C_D(\gamma^* + \theta)} = \cot\gamma^*, \quad (2.9)$$

where $\alpha^* = \gamma^* + \theta$. This transcendental equation for the equilibrium glide angle γ^* can have multiple solutions, which depend on the number of times the lift-to-drag ratio curve $\frac{C_L}{C_D}$ intersects the $\cot\gamma^*$ curve. Furthermore, the location and number of equilibria depend on the pitch angle θ. Because lift and drag are not analytical expressions of angle of attack, the equilibrium glide angle is found numerically. From equation (2.9), changing the pitch angle shifts the equilibrium glide angle, and to find these values, we consecutively shifted the lift-to-drag ratio curve over a range of specified pitch angles and used the Newton–Raphson root-finding method to locate the intersections. This technique is shown in figure 2, where two equilibrium glide states exist for a pitch of 10° and only one equilibrium for a pitch of −10°.
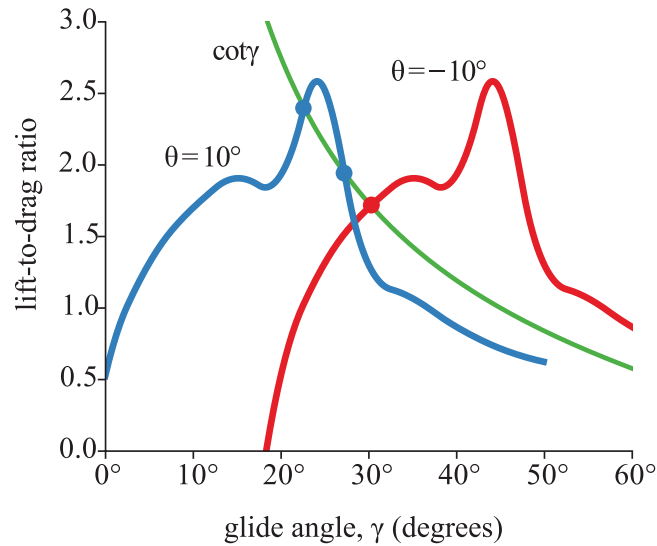
Figure 2. Pitch as a bifurcation parameter. Increasing the body pitch angle θ shifts the lift-to-drag ratio curves horizontally to the left, which changes the number of intersections with $\cot \gamma$. Each intersection is an equilibrium point, which are indicated by round markers at the intersection points for varying pitch angles. Force coefficient data are for a flying snake cross-sectional shape [8] at Re = 11 000.
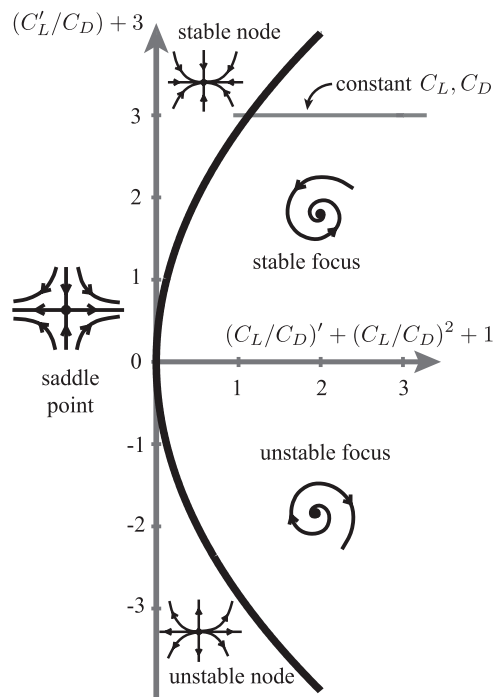

Figure 3. Summary of equilibrium type as a function of lift and drag curves. The equilibrium type is uniquely determined by the lift and drag curves and their slopes evaluated at the equilibrium angle of attack. Previous models of animal gliding, which assumed constant lift and drag coefficients, only observed stable node and stable focus type equilibrium points, as indicated by the horizontal gray line.

2.5. Equilibria type and stability analysis

To determine the stability type and location of equilibrium points in the velocity polar diagram, we use linear stability analysis [34] by classifying the eigenvalues of the Jacobian matrix of partial derivatives for the polar coordinate equations (2.7) and (2.8) evaluated at equilibrium. For this system of two equations, the eigenvalues $\lambda_{1,2}$ are

$$\lambda_{1,2} = \frac{C_D}{2(C_L^2 + C_D^2)^{1/4}} \left(-\tau \pm \sqrt{\tau^2 - 8\Delta} \right),$$

(2.10)

$$\tau = \left(\frac{C_L'}{C_D} \right) + 3$$

(2.11)

$$\Delta = \left(\frac{C_L}{C_D} \right)' + \left(\frac{C_L}{C_D} \right)^2 + 1$$

(2.12)

where $\left(\frac{C_L}{C_D} \right)'$ denotes the slope of the lift-to-drag ratio curve. The stability type depends on both the magnitude and slope of the lift and drag curves at equilibrium. This system permits five common types of equilibrium points, based on the signs and magnitudes of τ and Δ: stable and unstable foci, stable and unstable nodes, and saddle points. A summary of these equilibrium types is shown in figure 3.

If lift and drag coefficients are independent of angle of attack, then the primed terms in equations (2.11) and (2.12) are zero, and only stable equilibria are possible. That is, the simulated glider will never have a horizontal velocity of zero and will always reach an equilibrium with some horizontal velocity. Additionally, that equilibrium will be a stable focus if lift-to-drag ratio exceeds the low value of $\frac{1}{2\sqrt{2}} \approx 0.354$ ($\gamma^* > 70.53°$), and otherwise will be a stable node. If lift and drag coefficients are dependent on angle of attack, more dynamical behavior is possible.

2.6. Model input from experimentally measured lift and drag curves

To test the effect of angle-of-attack-dependent force coefficients and the applicability of the non-equilibrium gliding framework, we use aerodynamic coefficient curves (figure 4) from a range of animal gliders, including flying squirrel [20], flying snake [8],
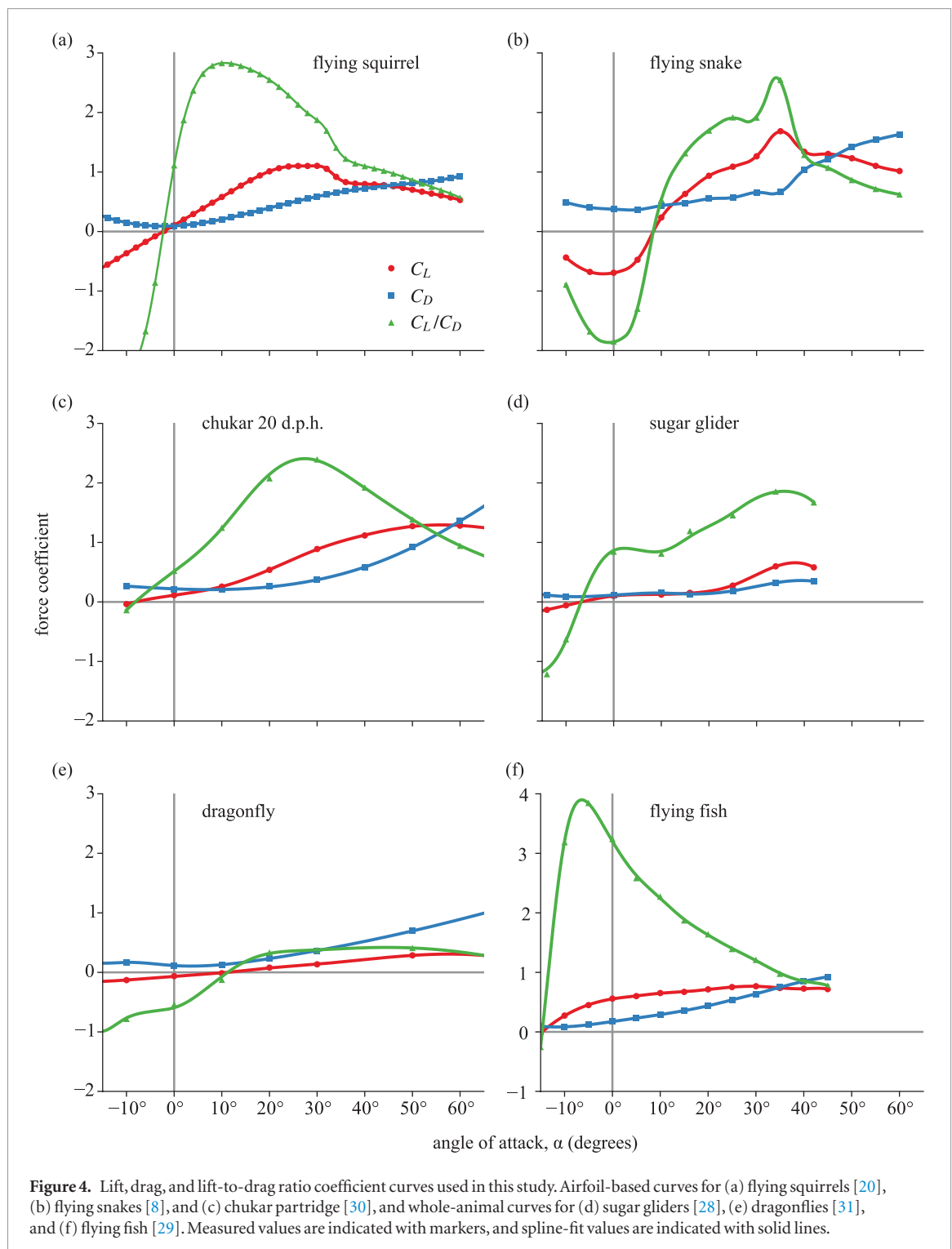
Figure 4. Lift, drag, and lift-to-drag ratio coefficient curves used in this study. Airfoil-based curves for (a) flying squirrels [20], (b) flying snakes [8], and (c) chukar partridge [30], and whole-animal curves for (d) sugar gliders [28], (e) dragonflies [31], and (f) flying fish [29]. Measured values are indicated with markers, and spline-fit values are indicated with solid lines.

sugar glider [28], and flying fish [29], as well as two active flyers, juvenile chukar partridge at 20 days post hatch (d.p.h.) [30], and dragonfly [31]. These species vary in size, Reynolds number, and aerodynamic force-producing structure. The chukar at 20 d.p.h can sustain level flight, but lacks the locomotor capacity of adults, as the wing is still developing and produces only small amounts of lift. Dragonflies use brief periods of gliding, lasting up to 0.5 s and covering 1 m. However, gliding is often interrupted by wingbeats, so glide durations are short (less than 0.2 s, mean of 0.13 s [31]). Coefficient curves are classified in three ways,

based on data from previous studies (table 1). The 'airfoil' curves are from wind tunnel experiments of a representative airfoil model. The 'whole animal' curves are from wind tunnel measurements of a deceased and taxidermically-prepared animal. The 'kinematics curves' are reconstructed from recorded glide trials of flying squirrels, and are further discussed below. The coefficient values were smoothed with third-order B-splines to provide a continuous representation for simulations and stability calculations.

Because the aerodynamic coefficients for the entire animal will be different from those of the airfoil alone [35],

Table 1. Types of force coefficient data used in this study. Details describing the derivation of the kinematic squirrel coefficients are presented in the supplemental information.

Animal	Data source	Description	Source
Flying squirrel	Airfoil	Latex membrane in a wind tunnel	[20]
Flying snake	Airfoil	Printed cross-section of *Chrysopelea paradisi* body	[8]
Chukar 20 d.p.h.	Airfoil	Juvenile *Alectoris chukar* wing	[30]
Sugar glider	Whole animal	*Petaurus breviceps papuanus* placed in wind tunnel	[28]
Dragonfly	Whole animal	*Calopteryx splendens* placed in wind tunnel	[31]
Flying fish	whole animal	*Cypselurus hiraii* placed in wind tunnel, model L2	[29]
Kinematic squirrel	Kinematics	Ensemble of *Glaucomys sabrinus* glides	[10]
Individual squirrel	Kinematics	Individual *Glaucomys sabrinus* glides	[10]

we also analyzed force coefficient curves (figure 7(a)) derived from kinematics measurements of flying squirrels gliding to a tree located 18 m from the launch platform [10]. These 'kinematics' coefficient curves were back-calculated from individual glides, as well as from an ensemble of all glides (see supplemental information). To reconstruct the angle-of-attack-dependent coefficients, first the force coefficients were calculated by rearranging equation (2.2). Second, the time-varying angle of attack was approximated as the sum of the calculated glide angle and an assumed pitch angle of zero degrees. We had to approximate the pitch angle because it was not available from the kinematics data. In general, the force coefficient curves measured from wind tunnel tests are of higher quality because (1) the velocities and angles of attack are precisely known, (2) they cover a wider angle of attack range, and (3) noise-magnifying numerical derivatives [36] are not present. Nonetheless, these coefficient curves were included to help synthesize theoretical predictions with observed glides.

2.7. Model assumptions

The complete non-equilibrium glide framework consists of the equations of motion, equations (2.5)–(2.8), and lift and drag coefficients determined from experiments. The model assumes angle-of-attack dependent, but velocity independent, quasi-steady lift and drag coefficients that are representative of the animal mid-glide. Although lift and drag coefficients are velocity independent, the lift and drag forces depend on the instantaneous velocity. Additionally, we do not explicitly model the rotational motion of the glider, but instead treat only one rotational direction, pitch, as a parameter that is systematically varied to elicit different glide performance. Finally, we treat motion in the vertical *x-z* plane only, ignoring side forces and

full three-dimensional glide trajectories resulting from yaw and roll rotations. The above assumptions provide the simplest model to explore the effect of angle-of-attack dependent lift and drag coefficients on a glider's trajectory dynamics.

3. Results

3.1. Structure of the velocity polar diagrams

Velocity polar diagrams for the airfoil and whole-animal-based lift and drag curves are shown in figure 5 for two different pitch angles. In these plots, initial conditions from the animal gliders originate near the origin of the diagram, with a near-zero vertical velocity and low horizontal velocity. These plots show that only certain equilibrium glides can be reached for the initial conditions typically observed in real glides. The velocity polar diagrams generally have multiple equilibria including stable nodes and saddle points. The stable and unstable manifolds of the saddle point delineate the basins of stability of stable glides. The upper stable branch of the saddle point, which runs vertically through the diagrams, acts as a separatrix (*sensu* Strogatz [34]) and can block accessibility to low glide angle equilibrium points. Additionally, saddles show that there are stable and unstable directions in the velocity polar diagram; these directions determine the glider's trend toward equilibrium.

Nearly all velocity trajectories in figure 5 (except for figure 5(dii)) fall quickly onto a one-dimensional manifold. If the trajectory originates in the basin of stability of the equilibrium point, the trajectory moves along the manifold and stable gliding is achieved. Otherwise, the trajectory is pushed to a steep glide where the horizontal velocity is low and the animal is in effect falling. The initial quick descent of the glider to the manifold corresponds to the ballistic phase of gliding (figures 1(d) and (g)), and movement along the manifold corresponds to the shallowing phase of gliding. We designate this one-dimensional manifold as the 'terminal velocity manifold' as it is a higher-dimensional analog of the terminal velocity, and dynamics along it are a relatively slow evolution toward stable equilibrium. The terminal velocity manifold is approximated by the curve of zero vertical acceleration, the v_z nullcline, along which equation (2.6) is zero. A trajectory in the vicinity of the nullcline would be in a near-vertical force balance, with the vertical component of the total aerodynamic force balancing the weight of the gliders. Nullclines are shown on the flying snake and chukar velocity polar diagrams (figures 5(bi), (ci), and (cii)). These curves pass through any equilibrium points present in the velocity polar diagram, and best approximate the terminal velocity manifold locally around the stable node. If a saddle point exists (e.g. figures 5(ai), (aii), (bii), (cii), and (fi)), then the terminal velocity manifold is also approximated by the unstable branch of a saddle point and the less-stable manifold of a stable node. Furthermore, we can
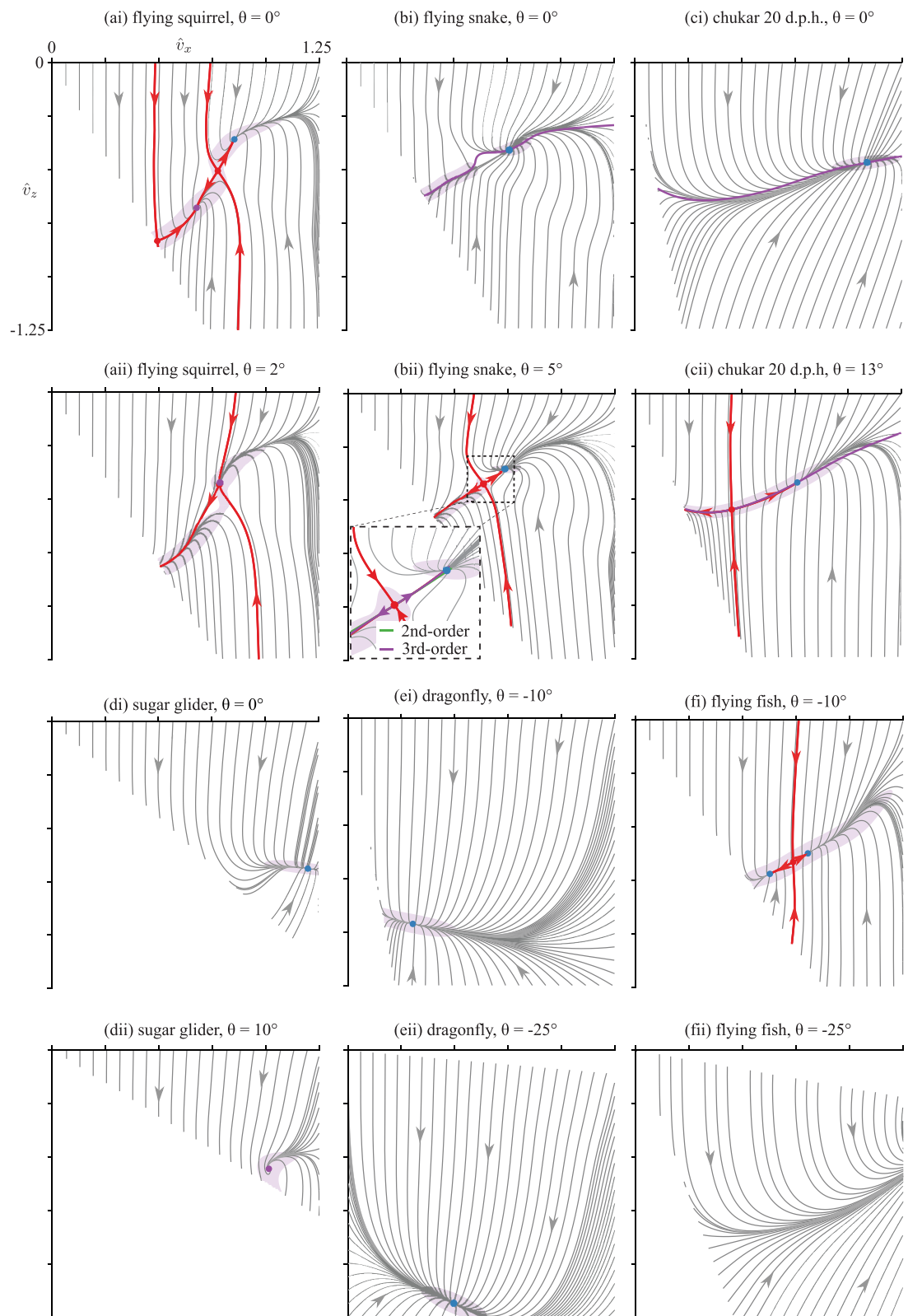
Figure 5. Velocity polar diagrams. Two different pitch values, indicated by (i) and (ii), are shown for (a) flying squirrels, (b) flying snakes, (c) chukar partridge, (d) sugar gliders, (e) dragonflies, and (f) flying fish. Pitch values are specified by vertical lines in figure 6. Gray lines are simulated glide trajectories, and arrows indicate motion along the trajectory through time. Equilibrium gliding is indicated by circle markers, and the glide angle is read as the angle subtended from the horizontal axis as before to the equilibrium point(s). Saddle points and their stable and unstable branches are indicated in red, with separatrices running vertically to the saddle points. The inset in (bii) shows 2nd and 3rd-order accurate analytical approximations of the terminal velocity manifold in the vicinity of the saddle point equilibrium. Vertical velocity nullclines, where the vertical acceleration is zero, are shown in (bi), (ci), and (cii), as the solid purple line passing though the equilibrium points and near the terminal velocity manifold. (ai) Flying squirrel, $\theta = 0$. (aii) Flying squirrel, $\theta = 2$. (bi) Flying snake, $\theta = 0$. (bii) Flying snake, $\theta = 5$. (ci) Chukar 20 d.p.h., $\theta = 0$. (cii) Chukar 20 d.p.h., $\theta = 13$. (di) Sugar glider, $\theta = 0$. (dii) Sugar glider, $\theta = 10$. (ei) Dragonfly, $\theta = -10$. (eii) Dragonfly, $\theta = -25$. (fi) Flying fish, $\theta = -10$. (fii) Flying fish, $\theta = -25$.

approximate the terminal velocity manifold analytically (see Supplemental Information), as shown in the inset of figure 5(bii).

Low-acceleration regions ($a \leqslant 0.1\,g$ where $a = \sqrt{a_x^2 + a_z^2}$) are identified by shading in all velocity polar diagrams in figure 5. These regions are located around the equilibrium points and along terminal velocity manifolds, which indicates that the glider will exhibit little change in velocity while far from equilibrium, with glide dynamics dictated by the direction of the manifold. Trajectories can also leave the low-acceleration region (figures 5(bi) and (bii)) while moving along the terminal velocity manifold towards equilibrium. In these velocity polar diagrams, this results from the peak in the lift-to-drag ratio of the flying snake coefficients near an angle of attack 35° (figure 4(b)).

3.2. Pitch bifurcation diagrams

The equilibrium points and corresponding equilibrium glide angles shown in figure 5 are summarized in a single bifurcation diagram for each glider in figure 6. For a given pitch angle, these diagrams show the stability type and glide angle of all possible equilibrium glides.

The bifurcation diagrams show multiple co-existing equilibrium points at high and low angles of attack, which persist over a range of pitch angles. The flying squirrel bifurcation diagram (figure 6(a)) shows that upwards of four co-existing equilibrium points are possible. In general, only a single stable equilibrium exists when pitch is negative, with equilibrium glide angles relatively insensitive to pitch. We refer to the slope of the pitch bifurcation curve along the branch of stable equilibrium points as the 'pitch sensitivity', calculated as $\mathrm{d}\gamma^*/\mathrm{d}\theta$. For the flying squirrel bifurcation diagram, a saddle-node bifurcation occurs at a maximum pitch of 2°. Beyond this pitch angle, no shallow equilibrium glides are observed, and the glider is essentially falling. The flying snake bifurcation diagram (figure 6(b)) is similar to the flying squirrel bifurcation diagram, except that more than four equilibria are possible at select pitch angles around 1°. The stable node and saddle point are much closer, and no equilibrium glides are found beyond the saddle-node bifurcation at a pitch angle of 12°.

The chukar, sugar glider, and dragonfly bifurcation diagrams (figures 6(c)–(e)) show a flat equilibrium glide angle region over a large range of pitch angles. Due to the low lift-to-drag ratio of the dragonfly, equilibrium glides are steep, being nominally 70° in glide angle. The flying fish and dragonfly bifurcation diagrams show that only negative pitch angles allow stable equilibria; in this condition, a flying fish or dragonfly would be nose-down at equilibrium.

3.3. Velocity polar diagrams from kinematics data

To demonstrate how these analytical methods can be applied to experimental data, we used mean force coefficients from a flying squirrel glide experiment

(figure 7(a)) as model inputs to construct both a bifurcation diagram (figure 7(b)) and velocity polar diagrams at zero and positive pitch values (figures 7(ci) and (cii)). The kinematic squirrel velocity trajectories show spiraling behaviors around both stable or unstable foci. This spiraling is also present in the velocity polar diagrams derived from individual glide trials (figures 7(d) and (e)), with the experimental velocity trajectory overlaid.

The kinematic squirrel bifurcation diagram (figure 7(b)) shows foci at low equilibrium glide angles that are insensitive to pitch; in particular, the equilibrium glide angle is almost constant from −5 to 4°. The two solid lines in this figure indicate the maximum and minimum glide angles of an unstable periodic orbit, which exists between Hopf bifurcation points at $\theta \approx -1°$ and $\theta \approx 5.6°$. This corresponds to the unstable periodic orbit in figure 7(ci) and the only closed contour in the velocity polar diagram. This Hopf bifurcation occurs any time the equilibrium changes from an unstable to a stable focus (and vice versa), and the characteristics of the resulting periodic orbit can be computed analytically given the lift and drag curves (see supplemental information).

4. Discussion

We have developed a dynamical systems framework to understand non-equilibrium animal gliding based only on the lift and drag coefficients. In this conceptualization of gliding, equilibrium is represented as a point in the velocity polar diagram where the accelerations are zero; trajectories will progress towards or away from equilibrium depending on the initial conditions and the equilibrium type. Analysis of the velocity polar diagram indicates that pitch angle has a large effect on the glide trajectory and that animal gliding has more complicated dynamics than previously realized. However, these dynamics can be systematically explored using the velocity polar diagram and by incorporating the lift and drag coefficient curves into the equation of motion.

4.1. Effect of lift and drag coefficients

Because lift and drag coefficients are the only model inputs, the analysis presented here can be viewed as a parametric study of representative lift and drag curves and how the structure of these curves affects non-equilibrium gliding. The analytically-derived expressions for equilibrium type (figure 3) and the general topology of the velocity polar diagrams (figure 5) indicate commonalities in how glide trajectories proceed based solely on the lift and drag curves. First, multiple equilibria are possible, and these generally occur for slightly negative to positive pitch values. Second, unstable equilibria are possible, particularly saddle points which appear along a terminal velocity manifold. Third, spiraling motion in the velocity polar
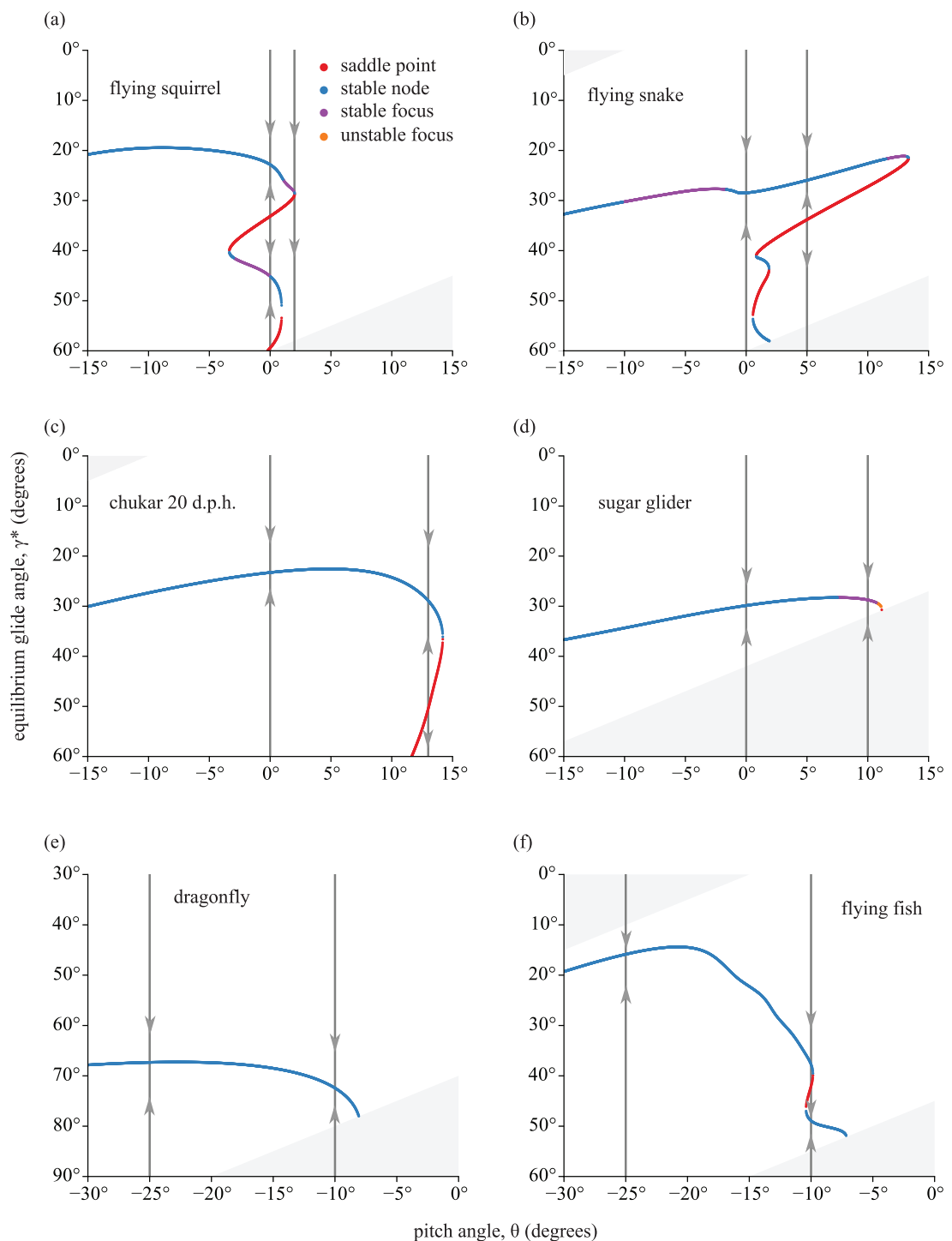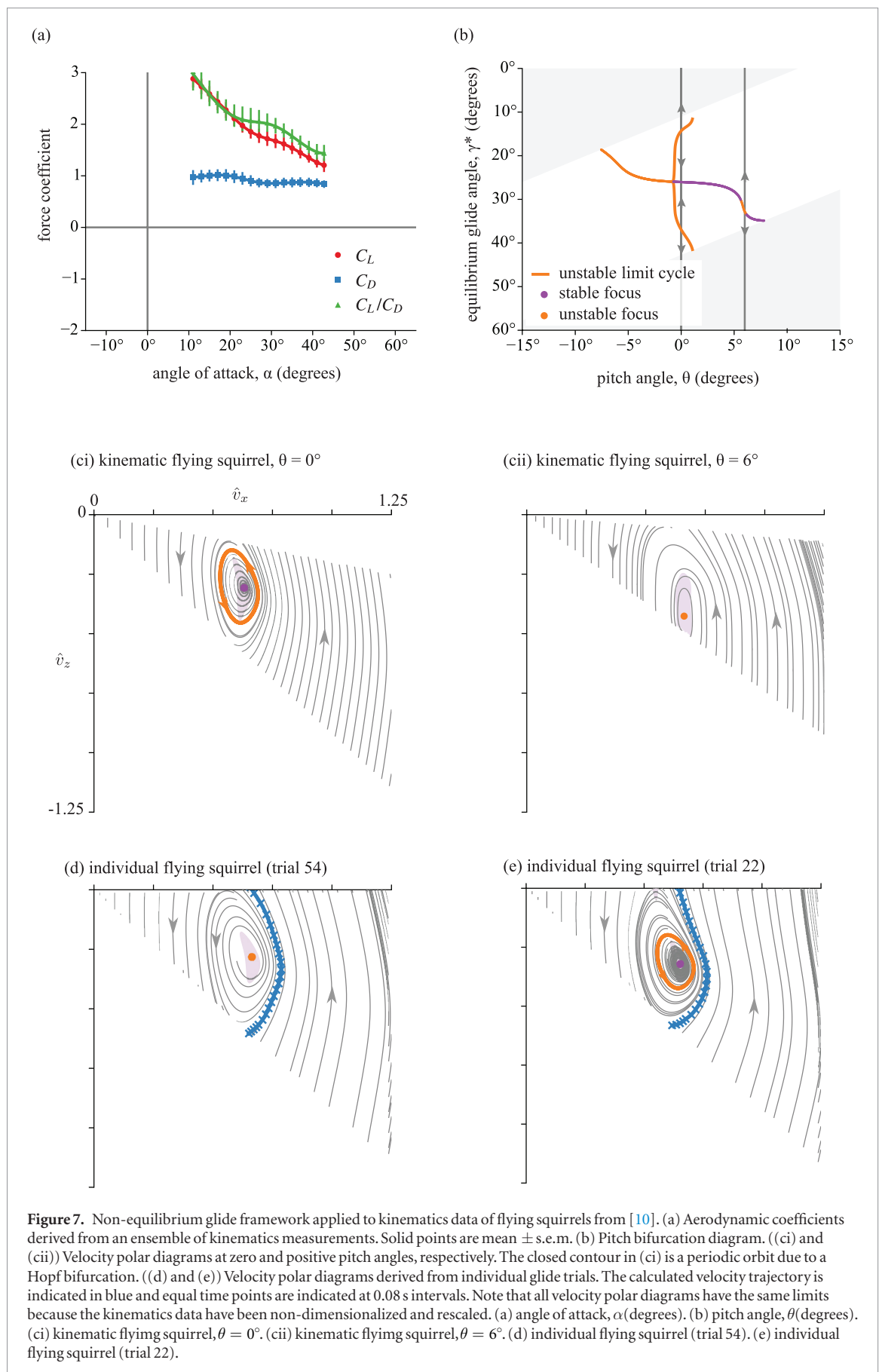
Figure 6. Pitch bifurcation diagrams for equilibrium glide angle γ^* as pitch angle θ varies. Diagrams correspond to (a) flying squirrels, (b) flying snakes, (c) chukar partridge, (d) sugar gliders, (e) dragonflies, and (f) flying fish. Equilibrium glide angles are found as intersection(s) of the bifurcation curve with vertical lines at a specified pitch angle, with multiple intersections indicating multiple equilibrium points. Colors correspond to different equilibrium types; cool colors are locally attracting and warm colors are locally repelling. Vertical lines indicate pitch angles used in the velocity polar diagrams in figure 5, and the arrows on these lines indicate the passive direction change of glide angle. Not all angles of attack were available in the original data; these regions are indicated with gray shading.

diagram is seen in several of the diagrams, particularly from the kinematics curves, but also when lift and drag coefficients are constants.

The difference in velocity polar diagram structure when there is a terminal manifold or when there is a focus-type equilibrium suggests future extensions of this work to investigate if gliders switch between dif-

ferent glide motifs. The motion around a focus-type equilibrium in the kinematics-based flying squirrel velocity polar diagrams (figures 7(c)–(e)), with a decrease in vertical velocity throughout the trajectory, is not seen in the airfoil-based velocity polar diagrams (figure 5). These different gliding motifs could provide complementary means to modify the glide path, but

Figure 7. Non-equilibrium glide framework applied to kinematics data of flying squirrels from [10]. (a) Aerodynamic coefficients derived from an ensemble of kinematics measurements. Solid points are mean ± s.e.m. (b) Pitch bifurcation diagram. ((ci) and (cii)) Velocity polar diagrams at zero and positive pitch angles, respectively. The closed contour in (ci) is a periodic orbit due to a Hopf bifurcation. ((d) and (e)) Velocity polar diagrams derived from individual glide trials. The calculated velocity trajectory is indicated in blue and equal time points are indicated at 0.08 s intervals. Note that all velocity polar diagrams have the same limits because the kinematics data have been non-dimensionalized and rescaled. (a) angle of attack, α (degrees). (b) pitch angle, θ (degrees). (ci) kinematic flyimg squirrel, $\theta = 0°$. (cii) kinematic flyimg squirrel, $\theta = 6°$. (d) individual flying squirrel (trial 54). (e) individual flying squirrel (trial 22).

how the animal switches between them is unknown. For example, the focus-based motif should lessen landing forces, because the vertical velocity is near zero or merely slightly positive at the end of the glide. However, the animal would have higher accelerations throughout the glide, which in theory would require more control

authority to maintain stability. In the terminal velocity manifold motif, accelerations are lower for the majority of the glide, but a large pitch-up maneuver would be required for landing to lower the airspeed. How the animal switches between these motifs with changes to lift and drag coefficients, or with unsteady aerodynamic and/or fluid-structure interaction effects [37–39], are important considerations for future work.

Calculating the kinematics-based lift and drag coefficient curves was done as a way to compare measured animal trajectories to model predictions. The velocity polar diagrams derived from wind tunnel measurements (figures 5(ai), (aii), (di), and (dii)) are substantially different from the kinematics-based ones (figures 7(c)–(e)). There are several possible reasons for this. One possibility is that the kinematics data are insufficient (due to undersampling, noise, or experimental error) to derive force coefficient curves. The kinematics data lack the ballistic phase of the glide, and the assumption of zero pitch angle used to derive the kinematics-based curves is likely to be invalid over part of the glide. Another possibility is that wind tunnel coefficient curves do not accurately represent the whole-animal aerodynamics in flight. This is most likely true for the artificial membrane curves, in which a thin latex sheet represents the patagial membrane, but does not include the limbs and tail of the flying squirrel. The sugar glider coefficient curves provide an intermediary to understand whole-animal lift and drag characteristics, as it is of a taxidermically prepared mammal in a likely flight configuration. In fact, these curves show spiraling in the velocity polar diagram (figure 5(dii)) for certain positive pitch angles, which is a likely flight posture used by flying squirrels [19]. Spiraling is also seen in the kinematics-based velocity polar diagrams in figures 7(c)–(e).

4.2. Comparison to other modeling studies of gliding

In the model presented here, the magnitude and orientation of the aerodynamic force vectors are modulated by pitch angle. Previous particle models were not directional, with the aerodynamic force vectors evolving under passive dynamics only [4, 5, 10, 25]. However, both types of models neglect rotational stability and consider translational motion assuming quasi-steady aerodynamics.
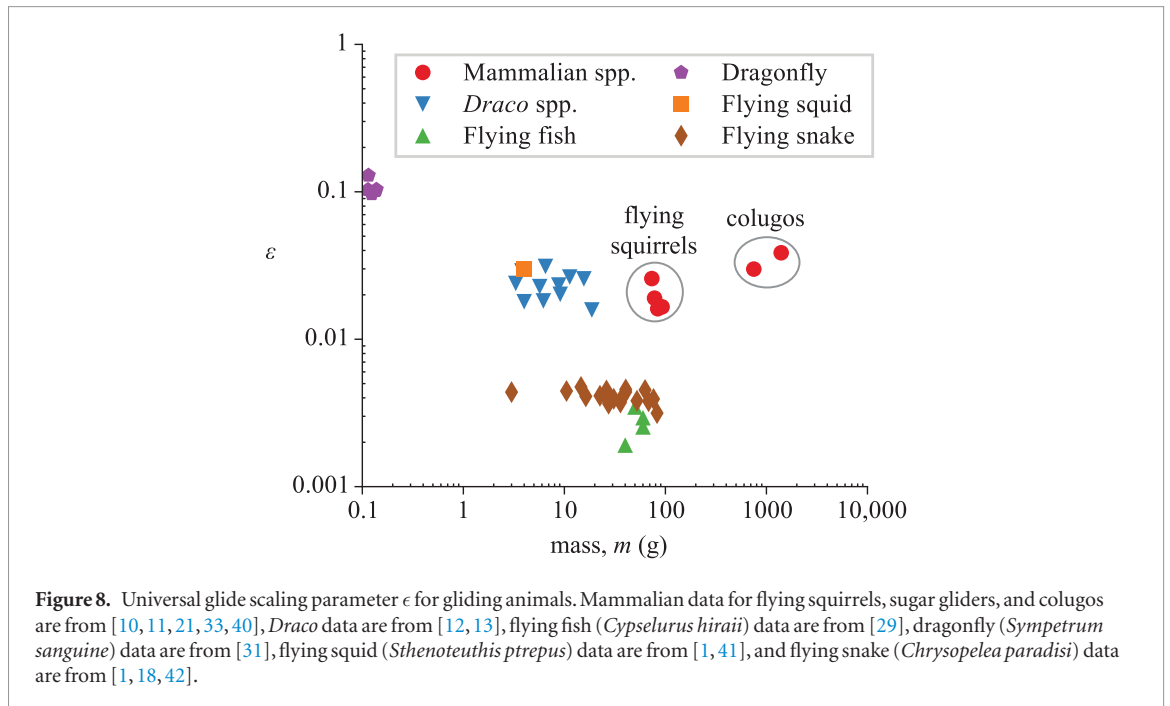
A significant difference between previous models and the model presented here is that lift and drag coefficients are not constants, but instead are angle of attack dependent. This difference results in drastically different simulated glide trajectories in both position and velocity space. When lift and drag coefficients are constants, only stable equilibria are possible, meaning that there are no physically realistic values of initial velocity or wing loading that result in falling directly downward. Additionally, these equilibria are predominantly of the focus type—the oscillatory behavior observed in previous models was a consequence of the lift-to-drag ratio only. This oscillatory behavior is very evident when

viewed in the velocity polar diagram (see figure 1 in the supplemental information). The glider does not smoothly transition from the ballistic phase to motion along the terminal velocity manifold, but instead oscillates towards an equilibrium glide.

When aerodynamic force coefficients depend on angle of attack, coexisting stable and unstable equilibrium points are possible. These equilibrium points organize the global topology of the velocity polar diagram and segregate regions that are reachable from typically low take-off velocities, rendering certain stable glide trajectories infeasible. Certain equilibria become inaccessible when a saddle point appears along the terminal velocity manifold. Because glides originate in the upper left quadrant of the velocity polar diagram, with near-zero vertical velocity and small horizontal velocity, the upper branch of the saddle point's stable manifold acts as a separatrix, which blocks low glide angle equilibrium points. The appearance of a saddle point explains the basin of stability observations in the $\theta_0 - \dot{\theta}_0$ space in previous snake modeling work [26], as certain initial condition combinations can lead to unsuccessful glides. In that previous study, the pitch rate affects the traversal of the non-autonomous velocity space, where this separatrix appears and blocks stable glides. This effect can also be understood as sweeping through pitch angle in the pitch bifurcation diagram in figure 6(b), where moving from negative to slightly positive pitch leads to a saddle-node bifurcation.

The newly presented non-dimensionalization and rescaling of the equations of motion is a significant difference from previous studies. This rescaling reduces the difference between species to their lift and drag coefficient curves only. The universal glide scaling parameter ($\epsilon \propto c/W_S$) not only facilitates modeling and normalization of experimental trajectories, but provides a metric to compare gliders based on their chord length and wing loading. Under geometric scaling of isometry, and assuming $c \propto L$ and $m \propto L^3$, one would expect chord length to scale as $c \propto m^{1/3}$. Experimental data suggest that wing loading scales isometrically, $W_S \propto m^{1/3}$ [1], so one would therefore expect $\epsilon =$ constant for a given species. The universal glide scaling parameter is shown in figure 8 for a variety of animal gliders across several orders of magnitude of mass. The scaling of ϵ with mass is not as evident as with wing loading [1], but there appear to be three distinct groupings. The first grouping has an ϵ value of 0.1 and includes dragonflies only. The next grouping has an ϵ of 0.04 and includes *Draco*, squid, and mammals. The third grouping, with an ϵ of 0.003, includes flying snakes and flying fish. For flying snakes, ϵ is nearly constant over two orders of magnitude in mass, and for *Draco*, ϵ is nearly constant over one order of magnitude in mass. These different scaling groups suggest that the chord length used to non-dimensionalize the equations of motion has a large effect on ϵ for different gliding species.

The universal glide scaling parameter also helps to explain why smaller individuals with lower wing loading are generally better gliders, covering more

Figure 8. Universal glide scaling parameter ϵ for gliding animals. Mammalian data for flying squirrels, sugar gliders, and colugos are from [10, 11, 21, 33, 40], *Draco* data are from [12, 13], flying fish (*Cypselurus hiraii*) data are from [29], dragonfly (*Sympetrum sanguine*) data are from [31], flying squid (*Sthenoteuthis ptrepus*) data are from [1, 41], and flying snake (*Chrysopelea paradisi*) data are from [1, 18, 42].

horizontal distance from a given take-off height. The framework presented here identifies equilibrium points in the velocity polar diagram, but it does not specify the time required to reach equilibrium. By converting both time and velocity back to physical units using ϵ,

$$t = \sqrt{\frac{2W_S}{\rho g^2}} \, \hat{t}, \qquad v = \sqrt{\frac{2W_S}{\rho}} \, \hat{v} \qquad (4.1)$$

we see that both dimensional time and velocity are proportional to the square root of wing loading. Because the time to equilibrium $\hat{t}$ is fixed in (4.1), the glider with lower wing loading will reach equilibrium sooner. If a large and a small individual were to take off from the same physical height and with the same initial conditions in the velocity polar diagram, the smaller individual would traverse more of the velocity space before landing. This would correspond with a higher shallowing rate, lower velocity, and greater horizontal distance traveled.

4.3. Implications for animals that glide
The global view of gliding developed here provides insight into how a glider's translational motion changes with pitch. The results of this work show that once the glider is at equilibrium, changing pitch angle has only a small effect on glide angle. For example, for the sugar glider (figure 6(d)), the equilibrium glide angles change only 10° over a pitch range of 25°. A similar trend holds for the other wind-tunnel based bifurcation diagrams, in which the low glide angle equilibrium is relatively insensitive to pitch. The initial launch parameters and the ballistic glide phase are therefore important because they determine how close to the basin of stability the glider is, and if control is needed to select a stable equilibrium. This analysis suggests that animals could select pitch values to avoid unstable features in the velocity polar diagram, with a worst-case scenario

resulting in a fall with negligible horizontal velocity. A negative pitch angle shortly after launch and through the ballistic phase will confer greater translational stability, and will also act to direct the lift vector horizontally.

Additionally, hysteresis effects are possible as the pitch angle changes. The equilibrium glide angle can increase rapidly if the pitch angle increases above a critical threshold (figures 6(a) and (b)). To re-establish a low glide angle equilibrium glide, a glider would have to decrease its pitch to a negative value so that only the upper stable branch of equilibria are possible. Therefore, a pitch-up maneuver prior to landing would not only slow the animal, but may remove all equilibria from the velocity polar diagram, so the animal would begin to fall. Only very steep glides are possible for some animals, such as dragonflies (figure 6(e)) and gliding arthropods. Arthropod glide trajectories consist of large glide angles between 70°–75° and small lift-to-drag ratio of approximately 0.3 [15–17]. Although lift and drag coefficient data are not available, these steep trajectories suggest velocity polar diagram structure similar to figure 5(e), with steep glides to a stable equilibrium.

The framework presented here also helps to address the question of if and when equilibrium is reached in gliding, as it clearly distinguishes true equilibrium where accelerations are zero, from equilibrium-like gliding in the shallowing phase and along the terminal velocity manifold where accelerations are small. Measured fluctuations of the glide path, which indicate non-equilibrium gliding, can occur for several reasons. One possibility is the animal in such a trajectory is using small postural changes to maintain a particular pitch angle or to slightly alter the glide path. Another possibility is that experimental errors, from digitization and numerical derivatives of position data, give the appear-

ance of spurious fluctuations. In either case, although its velocities and accelerations are changing, the glider is in effect confined to a region around equilibrium as it moves along the v_z nullcline and the terminal velocity manifold. The animal's trajectory in the velocity polar diagram, or its pitch angle history when viewing the pitch bifurcation diagram, can then be used to quantify the amount of non-equilibrium gliding and possibly control effort to maintain stability.

Lastly, the non-equilibrium gliding framework helps to elucidate the role of aerodynamic coefficients and airfoil performance on the evolution of flight. It has been previously suggested that phugoid gliding (long-wavelength oscillation of the glide trajectory) was used by the feathered dinosaur *Microraptor gui* [43]. These phugoid oscillations can be viewed as the position-space representation of a stable focus in the velocity polar diagram. Other phase-space structures, such as the terminal velocity manifold and the acceleration along it, likely confer other stability or energetic advantages. Detailed wind tunnel measurements of aerodynamic coefficients of *Microraptor gui* [44] can be used in the framework presented here to quantify how phase-space structures lead to variable glide performance between prehistoric and modern gliders.

5. Conclusions

We have presented a non-equilibrium framework of animal gliding based on the underlying structure in the equations of motion and empirically measured lift and drag coefficient curves. We find several structures in the velocity polar diagram relevant to gliders, including a terminal velocity manifold surrounded by low acceleration magnitude regions, saddle points that define the basin of stability of low glide angle equilibrium points, and equilibrium points of varying type and stability that affect glide performance. This framework not only clarifies previous modeling studies which assumed constant lift-to-drag ratio, but indicates how an animal can actively control its glide trajectory using pitch angle. New pitch bifurcation diagrams show how the equilibrium points change with pitch angle, and how the equilibrium points alter the structure of the velocity polar diagram during all phases of gliding. As more detailed kinematics data become available, this framework can be used to understand how experimentally recorded gliders alter their trajectory through control of body orientation and the likely drivers of this control. This framework also suggests that the glide dynamics of engineered aerial and aquatic autonomous gliders can be designed to exploit the structure of the velocity polar diagram. To exploit the structure of the velocity polar diagram would require designing angle-of-attack dependent lift and drag coefficients such that equilibria of known type, stability, and equilibrium glide angle are placed

in the velocity polar diagram. The autonomous glider would then only need small actuations in pitch angle to passively switch to different glide states.

References

[1] Socha J J, Jafari F, Munk Y and Byrnes G 2015 How animals glide: from trajectory to morphology *Can. J. Zool.* **93** 901–24

[2] Dudley R, Byrnes G, Yanoviak S P, Borrell B, Brown R M and McGuire J A 2007 Gliding and the functional origins of flight: biomechanical novelty or necessity? *Annu. Rev. Ecol. Evol. Systematics* **38** 179–201

[3] Vogel S 2009 *Glimpses of Creatures in Their Physical Worlds* (Princeton, NJ: Princeton University Press)

[4] Willis D, Bahlman J, Breuer K and Swartz S 2011 Energetically optimal short-range gliding trajectories for gliding animals *AIAA J.* **49** 2650–7

[5] Socha J J, Miklasz K, Jafari F and Vlachos P P 2010 Non-equilibrium trajectory dynamics and the kinematics of gliding in a flying snake *Bioinspiration Biomimetics* **5** 045002

[6] Socha J J 2011 Gliding flight in *Chrysopelea*: turning a snake into a wing *Integr. Comparative Biol.* **51** 969–82

[7] Miklasz K, LaBarbera M, Chen X and Socha J J 2010 Effects of body cross-sectional shape on flying snake aerodynamics *Exp. Mech.* **50** 1335–48

[8] Holden D, Socha J J, Cardwell N D and Vlachos P P 2014 Aerodynamics of the flying snake *Chrysopelea paradisi*: how a bluff body cross-sectional shape contributes to gliding performance *J. Exp. Biol.* **217** 382–94

[9] Krishnan A, Socha J J, Vlachos P P and Barba L A 2014 Lift and wakes of flying snakes *Phys. Fluids* **26** 031901

[10] Bahlman J W, Swartz S M, Riskin D K and Breuer K S 2013 Glide performance and aerodynamics of non-equilibrium glides in northern flying squirrels (*Glaucomys sabrinus*) *J. R. Soc. Interface* **10** 20120794

[11] Byrnes G, Lim N T-L and Spence A J 2008 Take-off and landing kinetics of a free-ranging gliding mammal, the Malayan colugo (*Galeopterus variegatus*) *Proc. R. Soc.* B **275** 1007–13

[12] McGuire J A 2003 Allometric prediction of locomotor performance: an example from southeast Asian flying lizards *Am. Nat.* **161** 337–49

[13] McGuire J A and Dudley R 2005 The cost of living large: comparative gliding performance in flying lizards (Agamidae: *Draco*) *Am. Nat.* **166** 93–106

[14] McCay M G 2001 Aerodynamic stability and maneuverability of the gliding frog *Polypedates dennysi J. Exp. Biol.* **204** 2817–26

[15] Yanoviak S P, Dudley R and Kaspari M 2005 Directed aerial descent in canopy ants *Nature* **433** 624–6

[16] Munk Y, Yanoviak S P, Koehl M A R and Dudley R 2015 The descent of ant: field-measured performance of gliding ants *J. Exp. Biol.* **218** 1393–401

[17] Yanoviak S P, Munk Y and Dudley R 2015 Arachnid aloft: directed aerial descent in neotropical canopy spiders *J. R. Soc. Interface* **12** 20150534

[18] Socha J J, O'Dempsey T and LaBarbera M 2005 A 3D kinematic analysis of gliding in a flying snake, *Chrysopelea paradisi J. Exp. Biol.* **208** 1817–33

[19] Paskins K E, Bowyer A, Megill W M and Scheibe J S 2007 Take-off and landing forces and the evolution of controlled gliding

in northern flying squirrels *Glaucomys sabrinus J. Exp. Biol.* **210** 1413–23

[20] Song A, Tian X, Israeli E, Galvao R, Bishop K, Swartz S and Breuer K 2008 Aeromechanics of membrane wings with implications for animal flight *AIAA J.* **46** 2096–106

[21] Bishop K L 2006 The relationship between 3D kinematics and gliding performance in the southern flying squirrel, *Glaucomys volans J. Exp. Biol.* **209** 689–701

[22] Vernes K 2001 Gliding performance of the Northern flying squirrel (*Glaucomys sabrinus*) in mature mixed forest of Eastern Canada *J. Mammal.* **82** 1026–33

[23] Zhukovskii N Y 1891 On soaring of birds *Tr. Otd. Fiz. Nauk Obs. lyubit. yestestvz.* **4** 2

[24] Andronov A A, Vitt A A and Khaikin S E 1966 *Theory of Oscillators* (Reading, MA: Addison-Wesley)

[25] Dyke G, de Kat R, Palmer C, van der Kindere J, Naish D and Ganapathisubramani B 2013 Aerodynamic performance of the feathered dinosaur *Microraptor* and the evolution of feathered flight *Nat. Commun.* **4** 2489

[26] Jafari F, Ross S D, Vlachos P P and Socha J J 2014 A theoretical analysis of pitch stability during gliding in flying snakes *Bioinspiration Biomimetics* **9** 025014

[27] Tucker V A 1998 Gliding flight: speed and acceleration of ideal falcons during diving and pull out *J. Exp. Biol.* **201** 403–14

[28] Nachtigall W, Grosch R and Schultze-Westrum T 1974 Gleitflug des Flugbeutlers *Petaurus breviceps papuanus* (Thomas) I *J. Comparative Physiol.* **92** 105–15

[29] Park H and Choi H 2010 Aerodynamic characteristics of flying fish in gliding flight *J. Exp. Biol.* **213** 3269–79

[30] Heers A M, Tobalske B W and Dial K P 2011 Ontogeny of lift and drag production in ground birds *J. Exp. Biol.* **214** 717–25

[31] Wakeling J M and Ellington C P 1997 Dragonfly flight I. Gliding flight and steady-state aerodynamic forces *J. Exp. Biol.* **200** 543–56

[32] Sunada S, Sakaguchi A and Kawachi K 1997 Airfoil section characteristics at a low Reynolds number *J. Fluids Eng.* **119** 129–35

[33] Bishop K L 2007 Aerodynamic force generation, performance and control of body orientation during gliding in sugar gliders (*Petaurus breviceps*) *J. Exp. Biol.* **210** 2593–606

[34] Strogatz S H 2001 *Nonlinear Dynamics and Chaos: with Applications to Physics, Biology, Chemistry, and Engineering* (Boulder, CO: Perseus Books)

[35] Milne-Thomson L M 1966 *Theoretical Aerodynamics* (New York: Dover)

[36] Walker J A 1998 Estimating velocities and accelerations of animal locomotion: a simulation experiment comparing numerical differentiation algorithms *J. Exp. Biol.* **201** 981–95

[37] Ern P, Risso F, Fabre D and Magnaudet J 2012 Wake-induced oscillatory paths of bodies freely rising or falling in fluids *Annu. Rev. Fluid Mech.* **44** 97–121

[38] Heisinger L, Newton P and Kanso E 2014 Coins falling in water *J. Fluid Mech.* **742** 243–53

[39] Vincent L, Scott Shambaugh W and Kanso E 2016 Holes stabilize freely falling coins *J. Fluid Mech.* **801** 250–9

[40] Stafford B J, Thorington R W Jr and Kawamichi T 2002 Gliding behavior of Japanese giant flying squirrels (*Petaurista leucogenys*) *J. Mammal.* **83** 553–62

[41] O'Dor R, Stewart J, Gilly W, Payne J, Borges T C and Thys T 2013 Squid rocket science: how squid launch into air *Deep-Sea Res* II **95** 113–8

[42] Socha J J and LaBarbera M 2005 Effects of size and behavior on aerial performance of two species of flying snakes (*Chrysopelea*) *J. Exp. Biol.* **208** 1835–47

[43] Chatterjee S and Jack Templin R 2007 Biplane wing planform and flight performance of the feathered dinosaur *Microraptor gui Proc. Natl Acad. Sci. USA* **104** 1576–80

[44] Evangelista D, Cardona G, Guenther-Gleason E, Huynh T, Kwong A, Marks D, Ray N, Tisbe A, Tse K and Koehl M 2014 Aerodynamic characteristics of a feathered dinosaur measured using physical models. Effects of form on static stability and control effectiveness *PLoS One* **9** e85203